

# A Wideband Microwave Tomography System With a Novel Frequency Selection Procedure

Colin Gilmore\*, *Member, IEEE*, Puyan Mojabi, *Student Member, IEEE*, Amer Zakaria, *Student Member, IEEE*, Majid Ostadrahimi, *Student Member, IEEE*, Cameron Kaye, Sima Noghianian, *Senior Member, IEEE*, Lotfollah Shafai, *Fellow, IEEE*, Stephen Pistorius, *Senior Member, IEEE*, and Joe LoVetri, *Senior Member, IEEE*

**Abstract**—In this paper, we describe a 2-D wideband microwave imaging system intended for biomedical imaging. The system is capable of collecting data from 3 to 6 GHz, with 24 coresident antenna elements connected to a vector network analyzer via a  $2 \times 24$  port matrix switch. As one of the major sources of error in the data collection process is a result of the strongly coupling 24 coresident antennas, we provide a novel method to avoid the frequencies where the coupling is large enough to prevent successful imaging. Through the use of two different nonlinear reconstruction schemes, which are an enhanced version of the distorted born iterative method and the multiplicative regularized contrast source inversion method, we show imaging results from dielectric phantoms in free space. The early inversion results show that with the frequency selection procedure applied, the system is capable of quantitatively reconstructing dielectric objects, and show that the use of the wideband data improves the inversion results over single-frequency data.

**Index Terms**—Biomedical electromagnetic imaging, electromagnetic tomography, inverse problems, microwave imaging.

## I. INTRODUCTION

MICROWAVE tomography (MWT) is a promising alternative or complementary biomedical diagnostic technique for conventional soft-tissue imaging modalities. MWT uses microwave scattering measurements in the frequency range of a few hundred megahertz up to a few gigahertz to quantitatively reconstruct the bulk electrical properties, i.e., the permittivity and effective conductivity of the object being imaged. Current or predicted advantages of MWT include the following.

- 1) its low cost and portability, especially relative to MRI and X-ray computed tomography (CT);
- 2) its use of safe nonionizing radiation;
- 3) its ability to image bulk electrical properties as a feature of tissue that is not imaged by most other modalities;
- 4) its ability, without the use of contrast agents, to quantitatively reconstruct frequency-dependent permittivity and conductivity profiles of living tissue as a way of identifying physiological conditions of those tissues.

One possible application of MWT is in the frequent monitoring of tissue for the early detection of disease. For example, there is evidence to suggest that up to 22% of breast cancers detected by repeated mammographic screening naturally regress [1], and the ability to monitor these cancers with nonionizing radiation would be very useful. Significant progress in microwave imaging has been made in the last decade, with experimental prototypes having been used for the imaging of excised pigs' legs [2], a canine heart [3], and breast tumors [4]. In addition, promising pilot studies for human breast imaging have been completed [5], [6].

In this paper, we present both: 1) a wideband (3–6 GHz) multiantenna MWT system and 2) a novel method to select the operating frequencies of the system such that coupling from the coresident antennas is minimized. The system operates at a small number of single frequencies to create quantitative images of the complex dielectric permittivity. To the best of our knowledge, this frequency range is a significant increase in frequency range over any previously reported MWT systems, e.g., see [2], and [7]–[9], and it is well known that multifrequency measurements lead to improvements in image quality, e.g., see [10]–[12]. As the system utilizes an array of 24 coresident antennas that are both directive and can be highly coupling, a naive selection of the operating frequencies does not lead to effective MWT imaging, and the frequency selection method outlined herein offers an improvement in imaging results.

Microwave scattering data are converted to images via one of two nonlinear inversion algorithms: an enhanced version of the distorted born iterative method (DBIM), and the multiplicative regularized contrast source inversion (MR-CSI) method. The use of nonlinear inversion algorithms is necessary because linearizing assumptions about wave propagation, which allow for much simpler imaging algorithms, do not accurately model the actual physics. We utilize two different inversion algorithms in order to better show the abilities of the frequency selection procedure and the MWT system. This paper is not intended as a comparison of the two inversion algorithms.

Manuscript received June 30, 2009; revised September 23, 2009. First published November 20, 2009; current version published March 24, 2010. This work was supported by the Western Economic Development Canada, by the Natural Sciences and Engineering Research Council of Canada, by the CancerCare Manitoba, by the Manitoba Hydro, and by the Canadian Foundation for Innovation. Asterisk indicates corresponding author.

\*C. Gilmore is with the Department of Electrical and Computer Engineering, University of Manitoba, Winnipeg, MB R3T 2N2, Canada, and also with the CancerCare Manitoba, Winnipeg, MB R3E 0V9, Canada (e-mail: cgilmore@ee.umanitoba.ca).

P. Mojabi, A. Zakaria, M. Ostadrahimi, C. Kaye, L. Shafai, and J. LoVetri are with the Department of Electrical and Computer Engineering, University of Manitoba, Winnipeg, MB R3T 2N2, Canada (e-mail: joe\_lovetri@umanitoba.ca).

S. Noghianian was with the Department of Electrical and Computer Engineering, University of Manitoba, Winnipeg, MB R3T 2N2, Canada. She is now with the Department of Electrical Engineering, University of North Dakota, Grand Forks, ND 58202-8382 USA.

S. Pistorius is with the CancerCare Manitoba, Winnipeg, MB R3E 0V9, Canada, and also with the Department of Physics and Astronomy, University of Manitoba, Winnipeg, MB R3T 2N2, Canada.

Color versions of one or more of the figures in this paper are available online at <http://ieeexplore.ieee.org>.

Digital Object Identifier 10.1109/TBME.2009.2036372

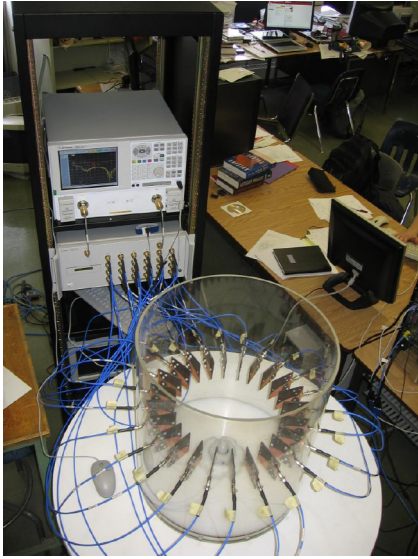


Fig. 1. Wideband MWT system. The 24 Vivaldi antennas are connected to a network analyzer via a  $2 \times 24$  switch.

Herein, we consider the MWT system operating in free space, although for planned future biomedical imaging, a matching fluid will need to be added to the system (which may necessitate the redesign of some components). We utilize dielectric targets that have contrasts similar to or greater than the contrasts expected for biomedical targets. The use of free space allows us to characterize the MWT system in an environment that is both more noisy (due to external noise) and more complicated than a system with a matching fluid. For example, a matching fluid will reduce both external noise sources and reduce the coupling between the antennas.

In its current configuration, the wideband MWT system assumes that both imaging targets and wave-field propagation is in 2-D. In this case, the  $E_z$  field is given by the scalar Helmholtz equation.

This paper is organized as follows. In Section II, we provide an overview of the MWT system and antennas. In Section III, we discuss the inversion problem formulation and the inversion algorithms. Section IV discusses the data collection and calibration, as well as the antenna-coupling analysis. In Section V, we show the inversion results for two different dielectric phantoms, followed by a discussion and conclusion.

## II. OVERVIEW OF SYSTEM

A photograph of the current prototype is shown in Fig. 1. We have employed a two-port Agilent 8363B PNA-series network analyzer (NA) as our microwave source and receiver, capable of producing measurements at discrete frequencies or sweeps within the required frequencies at an approximate system dynamic range of 122 dB (an additional 15 dB of dynamic range is available using the configurable test set). The NA is connected to the antennas with a  $2 \times 24$  cross-bar mechanical switch (Agilent 87050A-K24), which provides isolation of greater than 95 dB over the frequency range of interest. Twenty-four antennas are arranged at even intervals of  $15^\circ$  in a circular array at

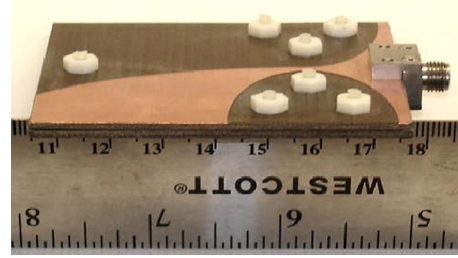


Fig. 2. Close up of one of the double-layered Vivaldi antennas used in the microwave imaging system. The two layers are held together with Teflon screws.

the midpoint height along the inside of a plastic cylinder. The cylinder has a radius of  $\approx 22$  cm, is 50.8 cm tall, and is water-tight, allowing it to be filled with a matching liquid (not utilized in this paper). The future use of a matching fluid may necessitate even higher isolation than 95 dB, and a redesign of the switch, but solutions to this do exist, e.g., see [13]. For use with certain classes of test targets, there is also a motor assembly located underneath the cylinder support structure that consists of two precision stepper motors arranged to provide accurate positioning of the target within the chamber. The test target may be placed on a plastic platform mounted on a central nylon pillar protruding from a water-tight, sealed hole in the center of the cylinder's bottom boundary, and can be rotated  $360^\circ$  (at increments smaller than  $1^\circ$ , if needed). A vertical movement range for the pillar of roughly 15 cm is also accommodated by the motor assembly to provide full 3-D positioning of the target through the 2-D plane of the antenna array.

Communication between the NA, switch, and the controlling computer is accomplished through the general-purpose interface bus (GPIB), operating via a GPIB-Ethernet hub. The data acquisition process is entirely automated. A full measurement at a single frequency ( $23 \times 24 = 552$  data points) takes less than 1 min (this time depends highly on the sweep time utilized for the NA). It is possible to further reduce this time, which will ultimately be limited by the stabilization time of the mechanical switch.

### A. Antenna Description

For this system, we utilize Vivaldi antennas [14], which have been specifically designed and improved for this near-field microwave imaging system [15]. The design bandwidth of the antennas is from 3 to 10 GHz, although, in practice, we have found them to be usable from 2 to 10 GHz. These antennas utilize a double-layer construction that significantly reduces the cross-polarization level of radiation pattern [15]. This is critical to the use of the scalar 2-D assumption about the wave propagation in the chamber, as antennas that create and detect  $x$ - and  $y$ -polarized fields would seriously degrade the resultant images. A picture of one of the antennas is shown in Fig. 2.

It is further desirable that these antennas have a radiation pattern as similar as possible to an ideal 2-D line-source ideal radiator, as this is the assumed source for the inversion algorithms used throughout. A plot of the gain pattern of a single antenna in the far-field region for the  $E_z$  polarization in the  $x$ - $y$

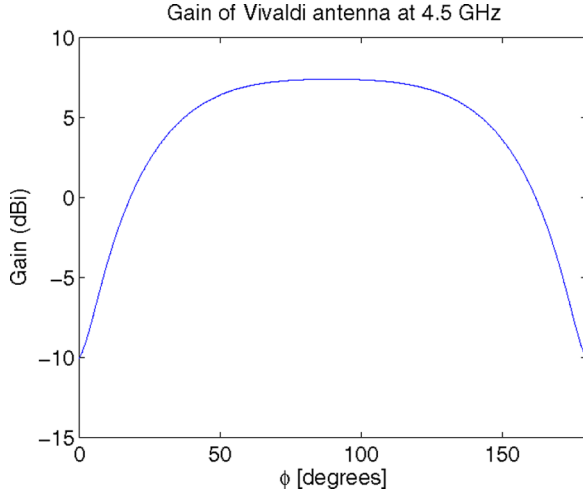


Fig. 3. Log-scale gain of the Vivaldi antenna in the  $H$ -plane.

plane is given in Fig. 3. The main beam has a  $70^\circ$  half-power beamwidth and is relatively flat across the center of the beam. While we expect this pattern to be significantly different inside the chamber (with the other coresident antennas), we experimentally choose specific frequencies at which the coupling to the other antennas is minimized. At these frequencies, we speculate that the incident field is reasonably close to that of an ideal 2-D line source inside the inversion domain.

The antennas are, however, more directive than a true 2-D line source. While this runs counter to the incident field assumption, it minimizes the coupling between the nearest nonactive antennas to the active (transmitting) antenna, which is also a problem for the inversion process.

### III. PROBLEM FORMULATION

Under the assumption of 2-D objects and field excitation, the total electric field in the  $z$  direction satisfies the scalar Helmholtz equation. The total field may be split into incident and scattered parts:  $E_z^{\text{tot}} = E_z^{\text{sct}} + E_z^{\text{inc}}$ , and the scattered field can be shown to satisfy [16]

$$[\nabla^2 + k_b^2(\mathbf{r})]E_z^{\text{sct}}(\mathbf{r}) = -k_b^2(\mathbf{r})\chi(\mathbf{r})E_z^{\text{tot}}(\mathbf{r}) \quad (1)$$

where  $k_b = \sqrt{\omega^2 \mu_0 \epsilon_b}$  is the background wavenumber, and the electric contrast is given by

$$\chi(\mathbf{r}) = \frac{\epsilon(\mathbf{r}) - \epsilon_b}{\epsilon_b} \quad (2)$$

where  $\epsilon_b$  is the complex permittivity of the background medium. The permittivities are taken to be complex so as to allow the modeling of both polarization and conductive losses. By assuming an  $e^{j\omega t}$  time dependency, the complex permittivity of an object may be written as

$$\epsilon(\mathbf{r}) = \epsilon'(\mathbf{r}) + j\epsilon''(\mathbf{r}) \quad (3)$$

where  $\epsilon''$  is the imaginary (lossy) part of the complex permittivity.

### A. Inversion Algorithms

In order to invert the data taken from this MWT system, we have implemented [17] two distinct inversion algorithms: the MR-CSI method [18], [19] and an enhanced version of the DBIM [20] (which is equivalent to the Gauss–Newton inversion method [21]). Both algorithms formulate the mathematical inverse problem as a nonlinear optimization problem that is iteratively solved for the complex permittivity of the unknown scatterer. The most significant difference between the two algorithms is that the enhanced-DBIM approach requires the repeated use of a forward solver, while the MR-CSI method does not.

Briefly, the DBIM method attempts to find the contrast that minimizes the objective function

$$F_{\text{DBIM}}(\chi) = \|\tilde{E}_z^{\text{sct}} - E_z^{\text{sct}}(\chi)\|_S^2 \quad (4)$$

where  $\tilde{E}_z^{\text{sct}}$  is the measured scattered field,  $E_z^{\text{sct}}$  represents the predicted scattered field from the estimated contrast  $\chi$ , and  $S$  denotes the measurement surface. The minimization is accomplished by approximating the function with a Taylor expansion and utilizing the Gauss–Newton optimization method. The process of regularization is critical to the success of the DBIM inversion method, and the details of the algorithm may be found in [17], [20], and [22].

On the other hand, the MR-CSI method seeks to minimize the objective function

$$F_{\text{CSI}}(\chi, w) = \frac{\|\tilde{E}_z^{\text{s}} - \mathcal{G}_S\{w\}\|_S^2}{\|\tilde{E}_z^{\text{s}}\|_S^2} + \frac{\|\chi E_z^{\text{inc}} - w + \chi \mathcal{G}_D\{w\}\|_D^2}{\sum_m \|\chi E_z^{\text{inc}}\|_D^2} \quad (5)$$

where  $\mathcal{G}_S$  and  $\mathcal{G}_D$  represent Green's function operators [19], the contrast sources are given by  $w(\mathbf{r}) = E_z(\mathbf{r})\chi(\mathbf{r})$ , and  $D$  denotes the domain where the scatterer is located. The CSI method forms two interlaced sequences in  $\chi$  and  $w$ , which are minimized by an interlaced application of the conjugate gradient method. The use of: 1) the different objective function and 2) two unknowns allows the objective function to be minimized without any external regularization, and without calling a forward solver.

Both inversion methods are further enhanced with a multiplicative regularizer (for details, see [17], [18], and [23]). The use of a multiplicative regularizer significantly enhances the performance of the inversion algorithms. With the use of the MR term, we call the DBIM approach the enhanced-DBIM approach.

### IV. DATA COLLECTION AND SYSTEM CALIBRATION

As the MWT inversion algorithms require scattered field measurements, and any physical system is only capable of detecting the total field, the raw data are first collected for the MWT system with no scatterer present. These data, labeled the “incident” measurement, are then subtracted from all the subsequent data to produce the scattered field data.



The scattered data must then be calibrated. There are two purposes for the calibration: 1) to convert the  $S_{21}$  values of the NA into  $E_z^{\text{tot}}$  ( $E_z$ ) field values used in the inversion algorithms and 2) to eliminate/compensate for as many measurement errors as possible. To perform the calibration, we first measure scattered data from a metallic cylinder with a known radius placed in the middle of the chamber. We denote these  $S$  parameters as  $S_{21}^{\text{sct,known}}$ . Next, the scattering experiment is repeated, but with the unknown target present. These  $S$  parameters are denoted  $S_{21}^{\text{sct,unknown}}$ . Assuming a 2-D line-source-generated incident field, we further denote the analytic scattered fields from the known metallic cylinder as  $u_{\text{known}}^{\text{sct}}$ . These values are calculated analytically [24].

Finally, the calibrated measured fields for the unknown target are calculated by

$$u_{\text{cal}}^{\text{sct}} = \frac{u_{\text{known}}^{\text{sct}}}{S_{21}^{\text{sct,known}}} S_{21}^{\text{sct,unknown}}. \quad (6)$$

This method of calibration will eliminate any errors that are constant over the two ( $S_{21}^{\text{sct}}$  known and unknown) measurements. Examples of these types of “removable” errors include cable losses and phase shifts, or mismatches at connectors. However, there are other factors in the measurement that are not constant between the two measurements, and thus, not entirely removed via the aforementioned calibration object. For example, the antenna factor is not guaranteed to be the same for the known and unknown measurements (as the system is operating in the near field). Another error that is not entirely compensated for is the antenna coupling, as the coupling will change when different scatterers are present in the chamber. For these reasons, the known object should be as similar as possible to the expected class of unknown target.

While some MWT systems utilize the “known” object to be the empty chamber (i.e., the incident measurement is utilized) [13], [25], we have found that the use of a metallic cylinder calibration object improves the inversion results for our system (see the results shortly). A well-characterized penetrable scatterer used for calibration would eliminate more systematic errors, and provide even better imaging results, but due to the ease of characterization, we have utilized a metallic cylinder.

## V. ANTENNA COUPLING AND FREQUENCY SELECTION PROCEDURE

In the current free-space configuration, one of the largest sources of error is the antenna coupling, which tends to change the radiation properties of the antennas. The coupling between the antennas will significantly change depending upon the total fields. As the total fields result from the scatterer inside the MWT system, the antenna coupling is a source of error that is not entirely removable by the calibration procedure.

To obtain usable frequencies for our inverse scattering experiments, we first measure the  $S_{11}$  parameter for a single antenna when no other antennas are present in the tank. This measurement is shown as the thick black line in Fig. 4. Next, the other 23 antennas are all placed in the MWT system, and the remaining

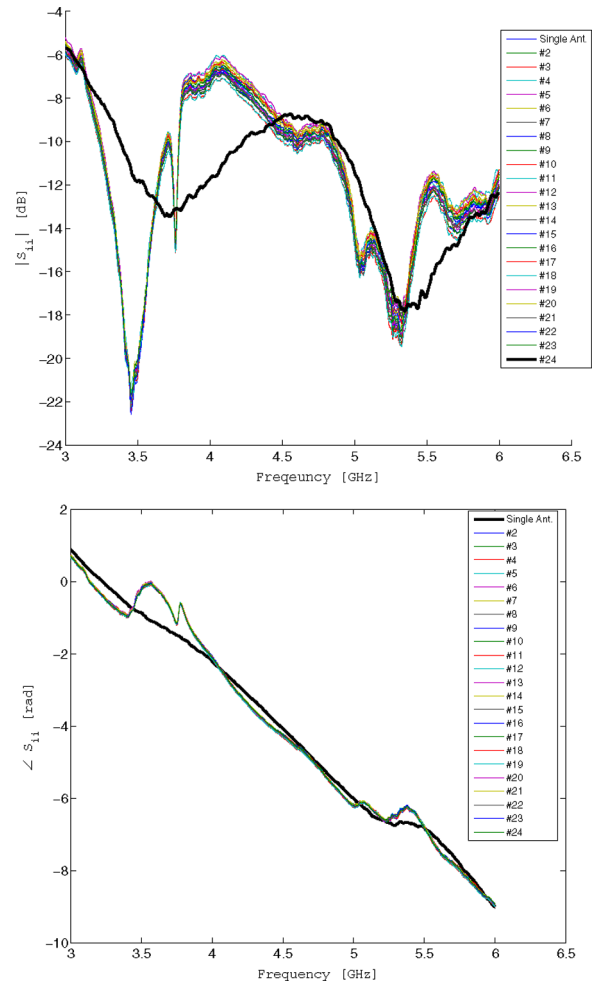


Fig. 4. Measurement of  $S_{ii}$  for Vivaldi antennas. (a)  $|S_{ii}|$ . (b)  $\text{Angle}(S_{ii})$ . The bold black line is a representative measurement when only a single antenna is present and the thin colored lines are the measurements for each antenna when all 24 antennas are coreisident in the tank.

$S_{ii}$  measurements are taken. These measurements are shown as the colored lines in Fig. 4.

The  $S_{ii}$  measurement of Fig. 4 provides an idea of where the antennas are strongly/weakly coupling. We have found this plot to be predictive of which frequencies will provide reasonable imaging results, and which frequencies will not. The usable-frequency selection is accomplished by avoiding the frequencies where there are large differences between the single antenna measurement and the coreisident measurement. For example, there is a significant difference between the single and coreisident measurements at 3.5 and 4 GHz, while there are much smaller differences at 3 and 4.5 GHz. In order to show the effects of these differences, in Figs. 5 and 6, we compare the analytic scattered fields from a metallic cylinder of radius 4.445 cm versus the calibrated measurement at 3, 3.5, 4, and 4.5 GHz. At the two frequencies where the coreisident  $S_{ii}$  measurements are significantly different than the free-space single  $S_{ii}$  antenna measurement (3.5 and 4 GHz), the calibrated measurements are much worse for both magnitude and phase. For example, the maximum relative error at 3.5 GHz is  $\approx 70\%$ , while

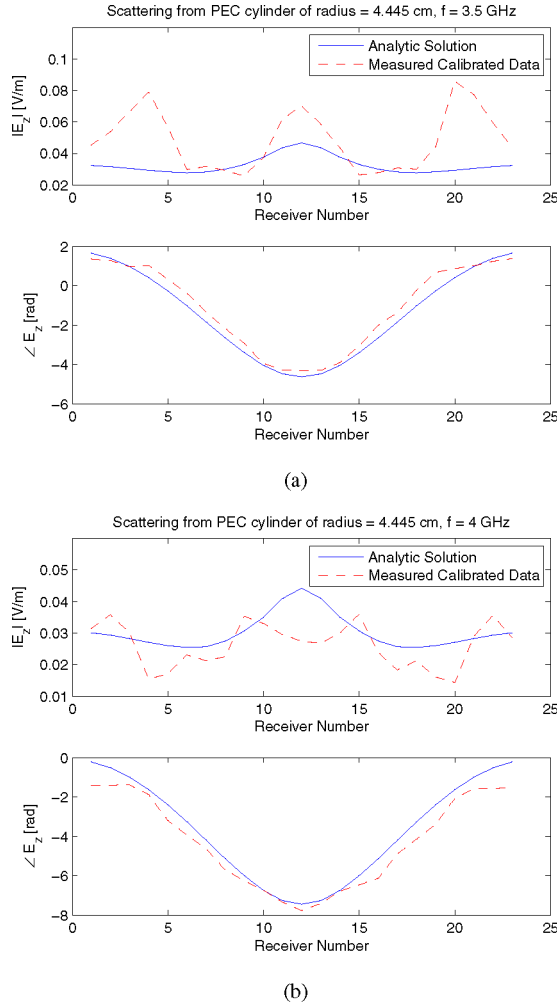


Fig. 5. Magnitude and phase comparison of scattered fields ( $E_z$ ) from a PEC cylinder at frequencies where the effects of antenna coupling are large. (a) 3.5 GHz. (b) 4 GHz. The solid blue line shows the analytic solution and the calibrated measured fields are shown with a dashed red line. The radius of the cylinder is 4.445 cm.

the maximum relative error at 3 GHz is  $\approx 20\%$ . These figures provide justification for the use of this basic method for avoiding the frequencies where the antennas are strongly coupling.

As is illustrated from Fig. 4, there are many more frequencies where the coupling is significant than minimal. Thus, in order to achieve a reasonable number of usable frequencies (e.g., 3), the wide bandwidth of the system is an important design feature.

We do note that even for the cases where the coupling seems to be minimal (see Fig. 6), there are still significant errors (e.g., at 4.5 GHz, the maximum relative error is  $\approx 25\%$ ). These errors are most likely due to the continued near-field coupling between the antennas, and the fact that the metallic scatterers used for the calibration of the system and  $S_{ii}$  comparison purposes were not true 2-D objects. This conjecture is based on the fact that other MWT systems with 2-D objects and far-field antennas do not see errors as large as this [26], [27]. We do note, however, that some near-field MWT systems have errors on the same order as this system [28]. For reference, the metallic cylinder used for calibration has a radius of 2.54 cm and is 65 cm tall, while the

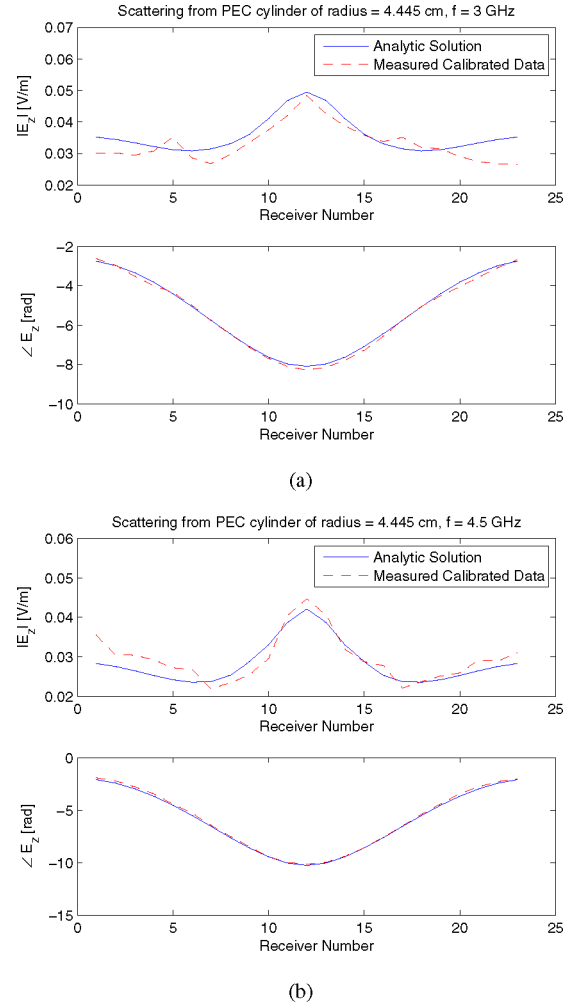


Fig. 6. Magnitude and phase comparison of scattered fields ( $E_z$ ) from a PEC cylinder at frequencies where the effects of antenna coupling are small. (a) 3 GHz. (b) 4.5 GHz. The solid blue line shows the analytic solution and the calibrated measured fields are shown with a dashed red line. The radius of the cylinder is 4.445 cm.

cylinder used for the comparison measurement has a radius of 4.445 cm and a height of 46 cm. Cylinders of different radii were selected to avoid calibrating and measuring the scattered fields with the same object, which would have provided an overly optimistic estimation of the experimental system accuracy.

## VI. RESULTS

For all experimental reconstructions, the only constraint on the minimization utilized was to keep the contrast within physical ranges (i.e.,  $\text{Re}(\chi) > 0$  and  $-\text{Im}(\chi) > 0$ ). This was accomplished by overwriting the values at the end of each iteration in the inversion process.

For the enhanced-DBIM method, we utilize a frequency-hopping approach for the multifrequency inversions. With the frequency-hopping scheme, data from each frequency are inverted independently, and the solution from the lower frequency is used as the initial guess for the next higher frequency [29], [30]. We have found the DBIM to be better suited

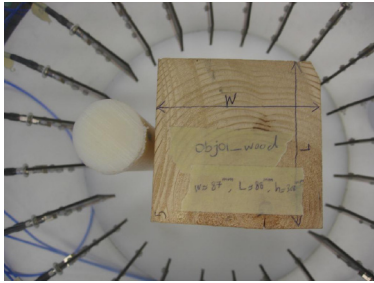


Fig. 7. Dielectric phantom target consisting of nylon and wooden cylinders.

to a frequency-hopping approach than a simultaneous multifrequency reconstruction, which we speculate is due to the use of the Born approximation as the initial guess, which is very problematic for the higher frequencies. For the MR-CSI method, we utilize a simultaneous multifrequency reconstruction (e.g., see [11] and [12]), where data from every frequency are utilized simultaneously. The data at each frequency are equally weighted. In our experience, the MR-CSI method produces better results with the simultaneous approach. These two different techniques are selected so that the best possible images from each class of algorithm are shown. The approximate time for a single-frequency inversion for the enhanced-DBIM algorithm is 23 min on a 2.66-GHz machine, and the MR-CSI inversion is 18 min on a 2.66-GHz machine.

#### A. Scatterer 1

As initial phantom experiments, we utilize a circular nylon-66 cylinder with a diameter of 3.8 cm (1.5 in) and an (approximately) square-cross-section wooden block. With the Agilent 85070E dielectric probe kit, we measured the wood to have a contrast of  $\chi^{\text{wood}} \approx 1.0 - j0.2$  at 3 GHz. As the nylon-66 cylinder is too small for accurate bulk-material measurement, we utilize the published contrast of  $\chi^{\text{nyl.}} = 2.0 - j0.03$  at 3 GHz [24].

Multifrequency probe measurements of these two targets has determined that lossy part of the permittivity increases as the frequency increases. This runs counter to the usual “Maxwell model” [18], [19], where  $\epsilon''(\mathbf{r}, \omega) = \sigma(\mathbf{r})/(\omega\epsilon_0)$ . We, therefore, assume a slightly better model where the lossy part of the dielectric does not vary with respect to frequency, i.e.,  $\epsilon''(\mathbf{r}, \omega) = \epsilon''(\mathbf{r})$ .

The targets were placed in the chamber, as shown in Fig. 7, with an air background, and  $23 \times 24$  measurements were taken for the frequencies of 3 and 6 GHz.

The single-frequency 3 GHz reconstruction from the enhanced-DBIM method is shown in Fig. 8(a) and (b), and the frequency-hopping-based reconstruction is shown in Fig. 8(c) and (d).

For the 3-GHz enhanced-DBIM reconstruction [see Fig. 8(a) and (b)], we note that the real part of the contrast shows the overall structure of the targets quite well, but the reconstruction for nylon is 20% low:  $\text{Re}(\chi_{\text{recon}}) = 1.6$  instead of the expected value of  $\text{Re}(\chi) = 2.0$ . For the wooden object, the real part of the contrast is reconstructed as  $\approx 1.1$ , within 10%, and the reconstruction shows a homogeneous region (which

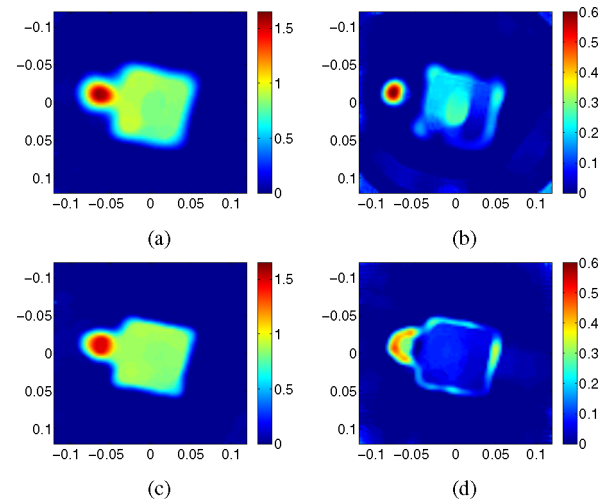


Fig. 8. (a)  $\text{Re}(\chi)$  and (b)  $-\text{Im}(\chi)$  show the enhanced-DBIM reconstruction of the dielectric phantom 1 at 3 GHz. (c) and (d) show the real and imaginary parts of  $\chi$  for DBIM reconstruction of the phantom using a frequency-hopping reconstruction at 3 and 6 GHz. Dimensions are in meters.

is what we expect). For the imaginary part of the enhanced-DBIM 3-GHz reconstruction, we note that the presence of the two distinct objects is clear, but the imaginary part of the nylon is overestimated ( $\text{Im}(\chi_{\text{recon}}) \approx -0.6$ , when it should be  $\text{Im}(\chi) = -0.03$ ). Further, the imaginary part of the contrast for the wooden object is not homogeneous, although the expected value of  $\text{Im}(\chi) = -0.2$  is achieved in the center.

For the 3- and 6-GHz enhanced-DBIM reconstruction, the contrast of the nylon is closer to the expected value than for the single-frequency case for the imaginary part ( $\text{Im}(\chi_{\text{recon}}) \approx -j0.45$ ). For the wood, the real part is again accurate (roughly the same as for the 3-GHz reconstruction). The edges of the objects are visible in the imaginary part of the reconstructed contrast, and the interior of the wood is more homogeneous, but the edges of the wood show some overshoot (in one particular spot,  $\text{Im}(\chi_{\text{recon}}) \approx -0.4$  when the expected value is  $-0.2$ ).

The single-frequency MR-CSI reconstruction at 3 GHz is shown in Fig. 9(a) and (b), and the simultaneous multifrequency reconstruction from 3 and 6 GHz data is shown in Fig. 9(c) and (d). Similar to the enhanced-DBIM case, the MR-CSI 3-GHz reconstruction underestimates the value of the nylon cylinder to be  $\text{Re}(\chi_{\text{recon}}) \approx 1.6$ , when it should be 2.0. The edges of the wood are not reconstructed as straight lines, and while the real part of the contrast is homogeneous, the value of the contrast is 15%, which is too low: ( $\text{Re}(\chi_{\text{recon}}) \approx 0.85$  instead of 1.0). For the imaginary part of the reconstruction, the contrast for the nylon is also overestimated ( $-0.6$  instead of  $-0.03$ ), and there is a point of high loss in the wood ( $-0.4$  instead of  $-0.2$ ).

In the multifrequency MR-CSI reconstruction [see Fig. 9(c) and (d)], the real part of the contrast underestimates the value of nylon, but is within 10% of the value for the wood (1.1). Additionally, the edges of the wood are much straighter. The imaginary part of the contrast does accurately show the presence of the nylon (i.e., shows a contrast of zero when it should be  $-0.03$ ), but all values of  $\text{Im}(\chi_{\text{recon}})$  are not overestimated. The

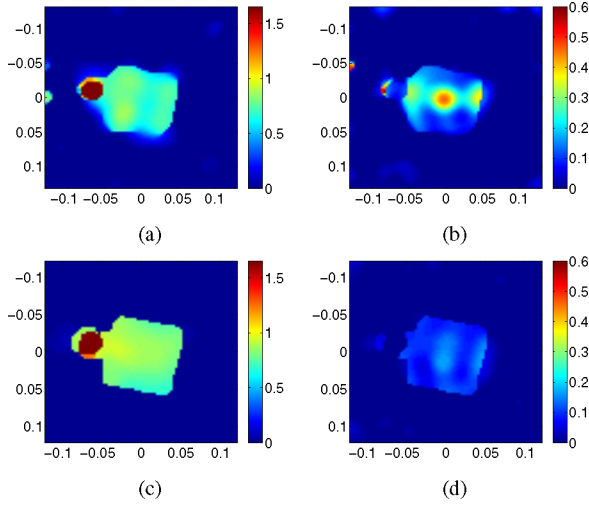


Fig. 9. (a)  $\text{Re}(\chi)$  and (b)  $-\text{Im}(\chi)$  show MR-CSI reconstruction for phantom 1 at 3 GHz. (c) and (d) show the real and imaginary parts of  $\chi$  for the MR-CSI reconstruction of phantom 1 using a simultaneous frequency reconstruction at 3 and 6 GHz. Dimensions are in meters.

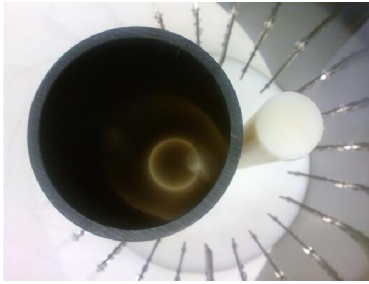


Fig. 10. Scatterer 2: Dielectric phantom target consisting of PVC and nylon cylinders. The separation between the cylinders was 1 cm.

reconstruction of the wood is again inhomogeneous in  $\text{Im}(\chi)$  reconstruction.

Finally, we also note that the off-axis rotation of the wood in all reconstructions reflects the physical orientation of the wood for the measurement.

### B. Scatterer 2

The second scatterer consists of the same nylon cylinder, but this time combined with a hollow polyvinylchloride (PVC) cylinder. A photograph of the phantom is shown in Fig. 10. The thickness of the PVC cylinder is  $\approx 0.6$  cm, and has a radius of  $\approx 6.5$  cm. The permittivity of the PVC cylinder was not measured, because the thin width of the cylinder wall would make the measurements invalid (the measurement would require a larger mass of PVC). However, published values [31] give the contrast of PVC at 3 GHz as  $\chi^{\text{PVC}} \approx 1.5 - j0.01$ .

For this phantom, data were collected at 3, 4.5, and 6 GHz. We show reconstructions at each individual frequency, as well as the full-frequency reconstructions. The enhanced-DBIM reconstruction at 3 GHz is shown in Fig. 11(a) and (b), the 4.5 GHz reconstruction is shown in (c) and (d), the 6 GHz reconstruction is shown in (e) and (f), and the marching-on-frequency recon-

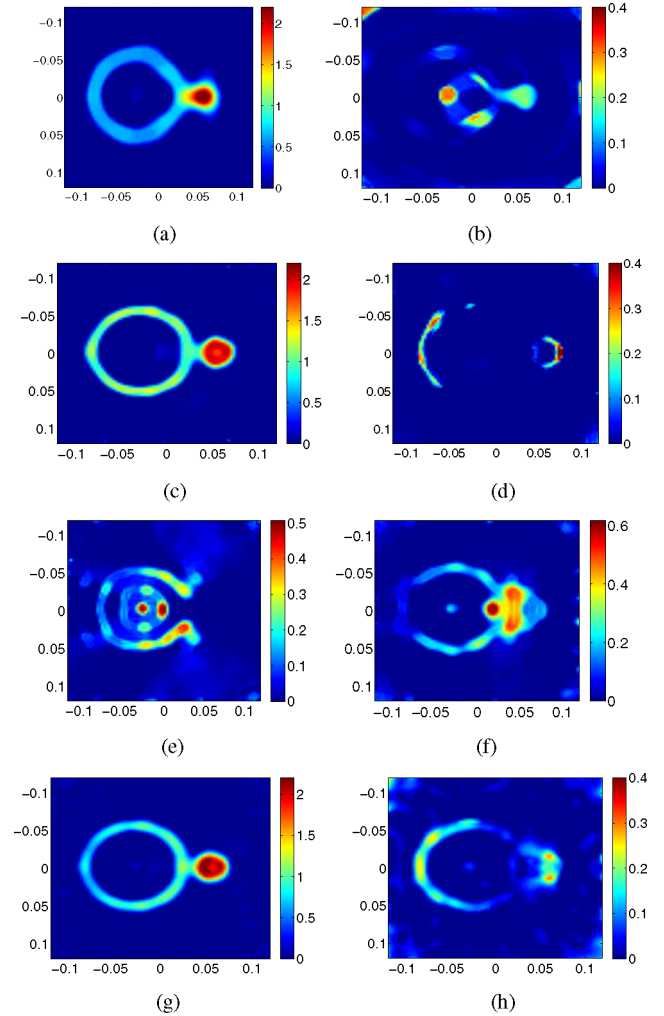


Fig. 11. Enhanced-DBIM reconstruction of scatterer 2. (a)  $\text{Re}(\chi)$  and (b)  $-\text{Im}(\chi)$  show the enhanced-DBIM reconstruction of the dielectric phantom 2 at 3 GHz. (c)  $\text{Re}(\chi)$  and (d)  $-\text{Im}(\chi)$  at 4.5 GHz. (e)  $\text{Re}(\chi)$  and (f)  $-\text{Im}(\chi)$  at 6 GHz. (g)  $\text{Re}(\chi)$  and (h)  $-\text{Im}(\chi)$  of the reconstruction using a marching-on-frequency reconstruction at 3, 4.5, and 6 GHz. Scales are not the same for each frequency, and dimensions are in meters.

struction is shown in (g) and (h). The MR-CSI reconstructions at the equivalent frequencies are shown in Fig. 12.

The enhanced-DBIM 3-GHz reconstruction [see Fig. 11(a) and (b)] overestimates the real part of the contrast for the nylon (2.2 instead of 2.0). The thickness of the PVC is estimated to be too wide ( $\approx 1.7$  cm instead of 0.6 cm). In the imaginary part of the enhanced-DBIM 3-GHz reconstruction, the overall structure of the phantom is not visible. This is mostly due to the large artifact in the center of the PVC pipe. The value of  $\text{Im}(\chi_{\text{recon}})$  for the nylon is  $-0.2$ , but the edges are blurred. The 4.5-GHz inversion shows some improvements, in that the reconstructed contrast of both the PVC and teflon are closer to the true values, although the imaginary part contains only a few edges, and the overall structure is not visible. The 6-GHz reconstruction has many artifacts and the inversion underestimates the real part of the contrast by 75%.

The multifrequency enhanced-DBIM reconstruction [see Fig. 11(c) and (d)] clearly shows the object in the real part



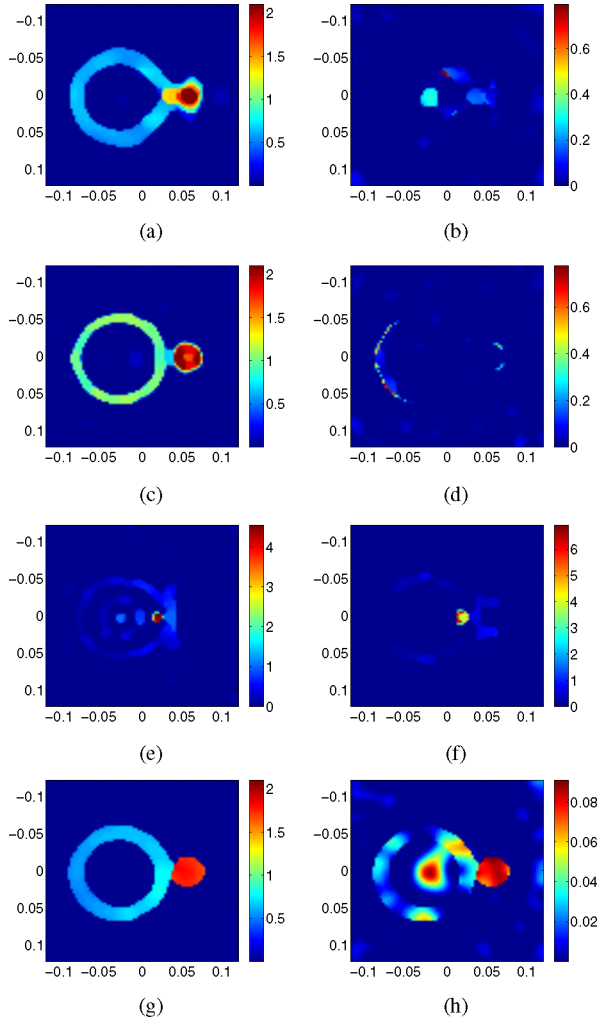


Fig. 12. MR-CSI reconstruction of the dielectric phantom 2. (a)  $\text{Re}(\chi)$  and (b)  $-\text{Im}(\chi)$  of the reconstruction at 3 GHz. (c)  $\text{Re}(\chi)$  and (d)  $-\text{Im}(\chi)$  at 4.5 GHz. (e)  $\text{Re}(\chi)$  and (f)  $-\text{Im}(\chi)$  at 6 GHz. (g)  $\text{Re}(\chi)$  and (h)  $-\text{Im}(\chi)$  of the reconstructions using a simultaneous frequency reconstruction at 3, 4.5, and 6 GHz. Scales are not the same for each frequency, and dimensions are in meters.

of the reconstruction, and the nylon cylinder is slightly overshoot. The real part of the PVC pipe reconstruction is thinner and closer to the actual size ( $\approx 1.2$  cm). In the imaginary part of the reconstruction, the nylon's shape is not really visible, and the value is overshoot ( $-0.3$  instead of  $-0.03$ ). Additionally, in the imaginary part of the PVC, pipe's shape does not follow the entire way around the cylinder.

In the 3-GHz single-frequency MR-CSI reconstruction, there is again an overestimate of the real part of the contrast for the nylon (2.3). The separation of the PVC and nylon is not at all clear and they are blurred together. The overall shape of the PVC cylinder is clear, but the thickness is overestimated ( $\approx 1.67$  cm instead of 0.6 cm). In the imaginary part of the MR-CSI single-frequency reconstruction, the overall structure is not visible, and there is a large artifact in the center of the inversion domain. The real part of the 4.5 GHz shows a closer fit to the actual size of the PVC, although the imaginary part of the reconstruction does not show the shape of the objects. The

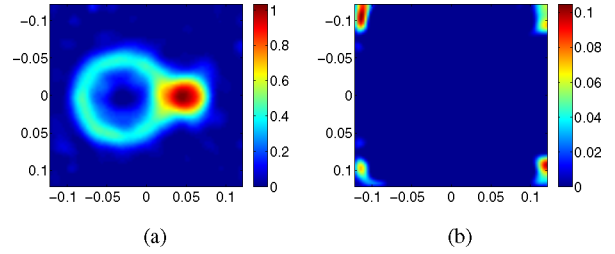


Fig. 13. Multifrequency (3–6 GHz) MR-CSI reconstruction of phantom 2, where the data were calibrated with the “incident field” calibration method. (a)  $\text{Re}(\chi)$ . (b)  $-\text{Im}(\chi)$ . Dimensions are in meters.

6-GHz reconstruction has significant overshoots in both real and imaginary reconstructions, and due to these, the shape of the target is not visible at this color scaling.

The multifrequency MR-CSI reconstruction shows slight undershoot in the real part of the nylon (1.8). The two objects are very distinct, although physically, the separation of 1 cm is not very distinct. The PVC is shown to be about 1.67 cm in width. The imaginary part of the reconstruction shows the nylon size (3.8 cm) and contrast quite accurately (i.e.,  $-0.1$  when it should be  $-0.13$ ). In the imaginary reconstruction, the PVC shape is visible, but does include some artifacts. Additionally, there still is a large artifact in the center of the imaging domain.

1) *Incident-Field-Based Calibration:* We utilize scatterer 2 to show the results of calibrating the MWT system with incident fields, as opposed to the normal method of calibrating the MWT system with the scattered fields from a metallic cylinder. For the incident field calibration, the quantities  $u_{\text{known}}^{\text{sct}}$  and  $S_{21}^{\text{sct,known}}$  in (6) are replaced with the incident field parameters:  $u_{\text{known}}^{\text{inc}}$  and  $S_{21}^{\text{inc,known}}$ . Excepting the calibration procedure, all other parameters were kept the same as for the previous cases.

The multi-frequency 3–6 GHz MR-CSI inversion results for scatterer 2 with incident field calibration are shown in Fig. 13. In this case, real part of the contrast is more blurred than for the usual case, and the peak value of the nylon cylinder is much lower than expected ( $\approx 1$ ). The imaginary part of the contrast consists entirely of artifacts.

### C. Discussion of Results

In both phantoms, the multifrequency reconstructions were an improvement over the single-frequency case. This is particularly apparent in the imaginary part of the permittivity of scatterer 2. As expected through the use of higher frequency data, the multifrequency reconstructions had less blurred edges. As well, in phantom 2, both the enhanced-DBIM and the MR-CSI multifrequency reconstructions clearly show that two distinct objects are present, and in the enhanced-DBIM case, the separation of the two objects is (arguably) visible (the physical separation was 1 cm, or  $1/5$  of  $\lambda$  at the highest frequency). The 6-GHz reconstructions of scatterer 2 show that the use of multifrequency data is important; we cannot simply invert the 6-GHz data and get the best result.

In general, the exact contrast/permittivity values were not obtained. For example, in the multifrequency MR-CSI reconstruction of phantom 2, the permittivity of the nylon is reconstructed



as  $\text{Re}(\chi_{\text{recon}}) = 1.8$ , when we expect it to be  $\text{Re}(\chi) = 2.0$ . The imaginary part of the permittivity is, in general, not accurately reconstructed, and there are many artifacts in the imaginary part of the reconstructions. This has been seen in other systems [8]. The problems in the imaginary part of the reconstructions were, however, improved with the use of multifrequency data.

We suspect that these errors in the reconstructions are primarily due to the large amount of measurement noise caused by the coupling of the antennas. Other sources of error, such as the assumption of a 2-D line-source-based incident field are probably less significant, and/or are adequately compensated for by the calibration process. We expect that when the MWT system is filled with a matching fluid, the antenna coupling will become significantly less noticeable due to losses in the fluid.

The results in Fig. 13 validate our use of a metallic cylinder as a calibration object (as opposed to the more common incident-field calibration method). For this particular system, the use of the metallic reference cylinder has provided better results, which may possibly be further improved through the use of a reference scatterer, which is even closer to the class of unknown scatterers to be imaged.

## VII. CONCLUSION

We have described an wideband microwave imaging system, capable of collecting data from 3 to 6 GHz. Furthermore, we have devised a simple method of avoiding the frequencies where the antenna coupling is too large for effective imaging, and utilized this method successfully in a complicated multiantenna environment. This simple method of selecting frequencies requires the wide-bandwidth of the system for effective operation. We have shown successful reconstructions of dielectric phantoms with contrasts similar or higher than those expected from biomedical targets. The results show that: 1) the collection of multifrequency data in a complex multiantenna environment is possible with a simple calibration procedure, as long as certain frequencies are avoided, and 2) images are improved by the use of this multifrequency data.

## REFERENCES

- [1] P.-H. Zahl, J. Mæhlen, and G. Welch, "The natural history of invasive breast cancers detected by screening mammography," *Arch. Intern. Med.*, vol. 168, no. 21, pp. 2311–2316, Nov. 2008.
- [2] S. Semenov, A. Bulyshev, A. Abubakar, V. Posukh, Y. Sizov, A. Souvorov, P. van den Berg, and T. Williams, "Microwave-tomographic imaging of the high dielectric-contrast objects using different image-reconstruction approaches," *IEEE Trans. Microw. Theory Tech.*, vol. 53, no. 7, pp. 2284–2294, Jul. 2005.
- [3] S. Y. Semenov, R. H. Svenson, V. G. Posukh, A. G. Nazarov, Y. E. Sizov, A. E. Bulyshev, A. E. Souvorov, W. Chen, J. Kasell, and G. P. Tastis, "Dielectrical spectroscopy of canine myocardium during acute ischemia and hypoxia at frequency spectrum from 100 KHz to 6 GHz," *IEEE Trans. Med. Imag.*, vol. 21, no. 6, pp. 703–707, Jun. 2002.
- [4] T. Rubæk, P. M. Meaney, P. Meincke, and K. D. Paulsen, "Nonlinear microwave imaging for breast-cancer screening using Gauss–Newton's method and the CGLS inversion algorithm," *IEEE Trans. Antennas Propag.*, vol. 55, no. 8, pp. 2320–2331, Aug. 2007.
- [5] P. M. Meaney, M. W. Fanning, T. Reynolds, C. J. Fox, Q. Fang, C. A. Kogel, S. P. Poplack, and K. D. Paulsen, "Initial clinical experience with microwave breast imaging in women with normal mammography," *Acad. Radiol.*, vol. 14, pp. 207–218, 2007.
- [6] S. Poplack, S. P. Poplack, T. D. Tosteson, W. A. Wells, B. W. Pogue, P. M. Meaney, A. Hartov, C. A. Kogel, S. K. Soho, J. J. Gibson, and K. D. Paulsen, "Electromagnetic breast imaging results of a pilot study in women with abnormal mammograms," *Radiology*, vol. 243, pp. 350–359, 2007.
- [7] Z. Q. Zhang and Q. H. Liu, "Three-dimensional nonlinear image reconstruction for microwave biomedical imaging," *IEEE Trans. Biomed. Eng.*, vol. 51, no. 3, pp. 544–548, Mar. 2004.
- [8] A. Fhager, P. Hashemzadeh, and M. Persson, "Reconstruction quality and spectral content of an electromagnetic time-domain inversion algorithm," *IEEE Trans. Biomed. Eng.*, vol. 53, no. 8, pp. 1594–1604, Aug. 2006.
- [9] P. Meaney, M. Fanning, D. Li, S. Poplack, and K. Paulsen, "A clinical prototype for active microwave imaging of the breast," *IEEE Trans. Microw. Theory Tech.*, vol. 48, no. 11, pp. 1841–1853, Nov. 2000.
- [10] O. Bucci, L. Crocco, T. Isernia, and V. Pascazio, "Inverse scattering problems with multifrequency data: Reconstruction capabilities and solution strategies," *IEEE Trans. Geosci. Remote Sens.*, vol. 38, no. 4, pp. 1749–1756, Jul. 2000.
- [11] A. Abubakar, P. M. van den Berg, and T. M. Habashy, "Application of the multiplicative regularized contrast source inversion method on TM- and TE-polarized experimental fresnel data," *Inverse Probl.*, vol. 21, pp. S5–S13, 2005.
- [12] Q. Fang, P. Meaney, and K. Paulsen, "Microwave image reconstruction of tissue property dispersion characteristics utilizing multiple-frequency information," *IEEE Trans. Microw. Theory Tech.*, vol. 52, no. 8, pp. 1866–1875, Aug. 2004.
- [13] D. Li, P. M. Meaney, T. Reynolds, S. A. Pendergrass, M. W. Fanning, and K. D. Paulsen, "Parallel-detection microwave spectroscopy system for breast imaging," *Rev. Sci. Instrum.*, vol. 75, pp. 2305–2313, Jul. 2004.
- [14] A. Abbosh, H. Kan, and M. Bialkowski, "Compact ultra-wideband planar tapered slot antenna for use in a microwave imaging system," *Microw. Opt. Technol. Lett.*, vol. 48, pp. 2212–2216, 2006.
- [15] M. Ostadrahimi, S. Noghianian, and L. Shafai, "A modified double layer tapered slot antenna with improved cross polarization," presented at the 13th Int. Symp. Antenna Technol. Appl. Electromagn. (ANTEM), Banff, AB, Canada, Feb. 15–18, 2009.
- [16] C. Gilmore, A. Abubakar, W. Hu, T. Habashy, and P. van den Berg, "Microwave biomedical data inversion using the finite-difference contrast source inversion method," *IEEE Trans. Antennas Propag.*, vol. 57, no. 5, pp. 1528–1538, May 2009.
- [17] C. Gilmore, P. Mojabi, and J. LoVetri, "Comparison of an enhanced distorted born iterative method and the multiplicative-regularized contrast source inversion method," *IEEE Trans. Antennas Propag.*, vol. 57, no. 8, pp. 2341–2351, Aug. 2009.
- [18] A. Abubakar, P. M. van den Berg, and J. J. Mallorqui, "Imaging of biomedical data using a multiplicative regularized contrast source inversion method," *IEEE Trans. Microw. Theory Tech.*, vol. 50, no. 7, pp. 1761–1777, Jul. 2002.
- [19] P. M. van den Berg and R. E. Kleinman, "A contrast source inversion method," *Inverse Probl.*, vol. 13, pp. 1607–1620, 1997.
- [20] W. C. Chew and Y. M. Wang, "Reconstruction of two-dimensional permittivity distribution using the distorted born iterative method," *IEEE Trans. Med. Imag.*, vol. 9, no. 2, pp. 218–225, Jun. 1990.
- [21] R. F. Remis and P. M. van den Berg, "On the equivalence of the Newton–Kantorovich and distorted Born methods," *Inverse Probl.*, vol. 16, pp. L1–L4, 2000.
- [22] J. D. Zaeytjij, A. Franchois, C. Eyraud, and J. Geffrin, "Full-wave three-dimensional microwave imaging with a regularized Gauss–Newton method—theory and experiment," *IEEE Trans. Antennas Propag.*, vol. 55, no. 11, pp. 3279–3292, Nov. 2007.
- [23] P. van den Berg, A. Abubakar, and J. Fokkema, "Multiplicative regularization for contrast profile inversion," *Radio Sci.*, vol. 38, pp. 23.1–23.10, 2003.
- [24] R. Harrington, *Time-Harmonic Electromagnetic Fields*. New York: IEEE Press, 2001.
- [25] C. Yu, M. Yuan, J. Stang, E. Bresslour, R. George, G. Ybarra, W. Joines, and Q. H. Liu, "Active microwave imaging ii: 3-D system prototype and image reconstruction from experimental data," *IEEE Trans. Microw. Theory Tech.*, vol. 56, no. 4, pp. 991–1000, Apr. 2008.
- [26] K. Belkebir and M. Saillard, "Testing inversion algorithms against experimental data: Inhomogeneous targets," *Inverse Probl.*, vol. 21, pp. S1–S3, 2005.
- [27] A. Litman and L. Crocco, "Testing inversion algorithms against experimental data: 3D targets," *Inverse Probl.*, vol. 25, pp. 020201–1–020201–5, 2009.

- [28] A. E. Bulyshev, A. E. Souvorov, S. Y. Semenov, V. G. Posukh, and Y. E. Sizov, "Three dimensional vector microwave tomography: Theory and computational experiments," *Inverse Probl.*, vol. 20, pp. 1239–1259, 2004.
- [29] W. C. Chew and J. H. Lin, "A frequency-hopping approach for microwave imaging of large inhomogeneous bodies," *IEEE Microw. Guided Wave Lett.*, vol. 5, no. 12, pp. 439–441, Dec. 1995.
- [30] Z. Peng and A. G. Tijhuis, "Transient scattering by a lossy dielectric cylinder: Marching-on-in-frequency approach," *J. Electromagn. Waves Appl.*, vol. 7, pp. 739–763, 1993.
- [31] M. Ken-Ichiro, A. Hanawa, and R. Nozaki, "Broadband complex permittivity measurement techniques of materials with thin configuration at microwave frequencies," *J. Appl. Phys.*, vol. 98, pp. 084107-1–084107-8, 2005.



**Colin Gilmore** (S'05–M'09) received the B.Sc. and the M.Sc. degrees in electrical engineering in 2002 and 2005, respectively, from the University of Manitoba, Winnipeg, MB, Canada, where he is currently working toward the Ph.D. degree in electrical engineering.

From 2002 to 2004, he was a Postgraduate Scholar of the Canadian Natural Sciences and Engineering Research Council (NSERC). From 2002 to 2008, he was an NSERC Canada Graduate Scholar. He is currently a Research Associate at the CancerCare

Manitoba, Winnipeg. His research interests include electromagnetic inversion, computational electromagnetics, and inverse problems.



**Puyan Mojabi** (S'09) received the B.Sc. degree in electrical and computer engineering from the University of Tehran, Tehran, Iran, in 2002 and the M.Sc. degree in electrical engineering from Iran University of Science and Technology, Tehran, in 2004. He is currently working toward the Ph.D. degree in electrical engineering at the University of Manitoba, Winnipeg, MB, Canada.

His research interests are computational electromagnetics and inverse problems.



**Amer Zakaria** (S'05) received the B.Sc. degree in electrical engineering (*summa cum laude*) from the American University of Sharjah, Sharjah, United Arab Emirates, in 2005, and the M.Sc. degree in microwave engineering (with high distinction) from Munich University of Technology, Munich, Germany, in 2007. He is currently working toward the Ph.D. degree in electrical engineering at the University of Manitoba, Winnipeg, MB, Canada.

His research interests include computational electromagnetics and inverse problems.



**Majid Ostadrahimi** (S'09) received the B.Sc. degree in electrical engineering from Sharif University of Technology, Tehran, Iran, in 2003, and the M.Sc. degree in electrical engineering from Iran University of Science and Technology, Tehran, in 2006. He is currently working toward the Ph.D. degree in electrical and computer engineering at the University of Manitoba, Winnipeg, MB, Canada.

His research interests include microwave imaging especially from the antenna and measurement point of view, dielectric measurement, and near-field mea-



resonant enclosures.

**Cameron Kaye** received the B.Sc. degree in computer engineering in 2005, and the M.Sc. degree in electrical engineering in 2009, both from the University of Manitoba, Winnipeg, MB, Canada.

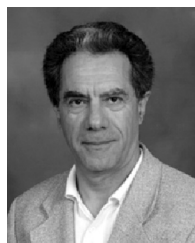
He is currently a member of the Faculty of Medicine, University of Manitoba, where he is also with the Microwave Imaging Research Group, Department of Electrical and Computer Engineering, and is engaged specifically in the development of microwave tomography prototypes. His research interests include calibration techniques for imaging within



**Sima Noghianian** (M'03–SM'05) received the M.Sc. and Ph.D. degrees in electrical engineering from the University of Manitoba, Winnipeg, MB, Canada, in 1996 and 2001, respectively.

From 2002 to 2003, she was an Assistant Professor in the Electrical Engineering Department, Sharif University of Technology. From 2003 to 2008, she was an Assistant Professor in the Electrical and Computer Engineering Department, University of Manitoba. She is currently an Assistant Professor in the Electrical Engineering Department, University of North

Dakota, Grand Forks. Her research interests include antenna design and modeling, wireless channel modeling, ultrawideband antennas, and microwave imaging.



**Lotfollah Shafai** (S'67–M'69–SM'75–F'88) received the B.Sc. degree from the University of Tehran, Tehran, Iran, in 1963, and the M.Sc. and Ph.D. degrees from the Faculty of Applied Sciences and Engineering, University of Toronto, Toronto, ON, Canada, in 1966 and 1969, respectively, all in electrical engineering.

Since 1969, he has been with the University of Manitoba, Winnipeg, MB, Canada, where he was a Sessional Lecturer in the Department of Electrical and Computer Engineering during November 1969,

an Assistant Professor in 1970, an Associate Professor in 1973, and a Professor in 1979, has been engaged in linking the University research to the industrial development since 1975, by assisting industries in the development of new products or establishing new technologies, assisted in establishing "The Institute for Technology Development," in 1985 to enhance the University's contact with industry, where he was the Director until 1987, and then became the Head of the Electrical Engineering Department, was the Industrial Research Chair in Applied Electromagnetics at the University of Manitoba from 1989 to July 1994, and was a Distinguished Professor during 2002.

He has been a participant in nearly all Antennas and Propagation Symposia and participates in the review committees. He was a Fellow of The Royal Society of Canada in 1998 and The Canadian Academy of Engineering. He is a member of Union Radio-Scientifique Internationale Commission B and was the Chairman during 1985 to 1988 and 2005 through 2008. In 1986, he established the symposium on Antenna Technology and Applied Electromagnetics at the University of Manitoba, which is currently held every two years. He has been a recipient of numerous awards. His contribution to the design of a small ground station for the Hermus satellite was selected as the 3rd Meritorious Industrial Design in 1978. He received the Professional Engineers Merit Award in 1984, "The Thinker" Award from Canadian Patents and Development Corporation in 1985, the "Research Awards" in 1983, 1987, and 1989 from the University of Manitoba, the Outreach Award in 1987 and the Sigma Xi, Senior Scientist Award in 1989, the Maxwell Premium Award from the Institute of Electrical Engineers (London) in 1990, the Distinguished Achievement Awards from Corporate Higher Education Forum in 1993 and 1994, the Winnipeg RH Institute Foundation Medal for Excellence in Research in 1998, the University of Manitoba, Faculty Association Research Award in 1999 and 2000, the IEEE Third Millennium Medal in 2000, and an IEEE Canada "Reginald A. Fessenden Medal" for "Outstanding Contributions to Telecommunications and Satellite Communications," and a Natural Sciences and Engineering Research Council Synergy Award for the "Development of Advanced Satellite and Wireless Antennas" in 2003. He was a Fellow of the Engineering Institute of Canada in 2009 and was the recipient of an IEEE Chen-To-Tai Distinguished Educator Award.



**Stephen Pistorius** (M'01–SM'08) received the B.Sc. degree from the University of Natal, Durban, South Africa, in 1982, and the B.Sc. (Hons.) degree in radiation physics, the M.Sc. degree in medical science, and the Ph.D. degree in physics from the University of Stellenbosch, Stellenbosch, South Africa, in 1983, 1984, and 1991, respectively.

He is currently the Provincial Director of medical physics at CancerCare Manitoba, Winnipeg, MB, Canada. He is a Full Professor of physics and astronomy, and an Associate Professor of radiology in the

University of Manitoba, Winnipeg. His current research interests include cancer imaging for both early detection and optimized radiation therapy. He is the author or coauthor of more than 100 publications and presentations.

Prof. Pistorius is a certified Medical Physicist. He was the President of the Canadian Organization of Medical Physics, the Coordinator of the Commission on Accreditation of Medical Physics Educational Programs accredited Medical Physics Graduate Program at the University of Manitoba, and is currently the Director of Professional Affairs for the Canadian Association of Physicists. He has received a number of national and international awards.



**Joe LoVetri** (S'84–M'84–SM'09) was born in Enna, Italy, in 1963. He received the B.Sc. (with distinction) and M.Sc. degrees in electrical engineering from the University of Manitoba, Winnipeg, MB, Canada, in 1984 and 1987, respectively, and the Ph.D. degree in electrical engineering from the University of Ottawa, Ottawa, ON, Canada, in 1991.

From 1984 to 1986, he was the Electromagnetic Interference/Electromagnetic Compatibility Engineer at Sperry Defence Division, Winnipeg. From 1986 to 1988, he was the Telecommunications Electronics

Material Protected From Emanating Spurious Transmissions Engineer at the Communications Security Establishment, Ottawa. From 1988 to 1991, he was a Research Officer at the Institute for Information Technology, National Research Council of Canada. From 1991 to 1999, he was an Associate Professor in the Department of Electrical and Computer Engineering, The University of Western Ontario. From 1997 to 1998, he spent a sabbatical year at the TNO Physics and Electronics Laboratory, The Netherlands. Since 1999, he has been a Professor in the Department of Electrical and Computer Engineering, University of Manitoba, where he was an Associate Dean, Research, from 2004 to 2009. His current research interests include time-domain computational electromagnetics, modeling of electromagnetic compatibility problems, microwave tomography, and inverse problems.